

# Evaporation of droplets capable of bearing viruses airborne and on hydrophobic surfaces

Cite as: J. Appl. Phys. **129**, 024703 (2021); <https://doi.org/10.1063/5.0023501>

Submitted: 30 July 2020 . Accepted: 23 December 2020 . Published Online: 12 January 2021

 Md Syam Hasan,  Konstantin Sobolev, and  Michael Nosonovsky



View Online



Export Citation



CrossMark



## Your Qubits. Measured.

Meet the next generation of quantum analyzers

- Readout for up to 64 qubits
- Operation at up to 8.5 GHz, mixer-calibration-free
- Signal optimization with minimal latency

Find out more



# Evaporation of droplets capable of bearing viruses airborne and on hydrophobic surfaces

Cite as: J. Appl. Phys. 129, 024703 (2021); doi: 10.1063/5.0023501

Submitted: 30 July 2020 · Accepted: 23 December 2020 ·

Published Online: 12 January 2021



View Online



Export Citation



CrossMark

Md Syam Hasan,<sup>1</sup>  Konstantin Sobolev,<sup>2</sup>  and Michael Nosonovsky<sup>1,a)</sup> 

## AFFILIATIONS

<sup>1</sup>Department of Mechanical Engineering, University of Wisconsin-Milwaukee, 3200 N Cramer St., Milwaukee, Wisconsin 53211, USA

<sup>2</sup>Department of Civil and Environmental Engineering, University of Wisconsin-Milwaukee, 3200 N Cramer St., Milwaukee, Wisconsin 53211, USA

<sup>a)</sup>Author to whom correspondence should be addressed: nosonovs@uwm.edu. Tel.: +1-414-229-2816

## ABSTRACT

Airborne and deposited water microdroplets can carry viruses including coronaviruses. The evaporation of microdroplets containing virus particles often leads to virus inactivation. Microdroplet evaporation involves various mechanisms such as diffusion, the Kelvin effect, infrared irradiation, and the role of solutes. For the evaporation of airborne water microdroplets, temperature and relative humidity of ambient air are important factors. However, for sessile droplets deposited on solid surfaces, wetting and porosity become important factors that control evaporation on regular, superhydrophobic, and photocatalytic surfaces. An experimental study of the effect of wetting properties and porosity on the evaporation rates on the polypropylene non-woven medical fabric was consistent with the theoretical models. Highly porous tile surfaces exhibited 2.2–4 times faster evaporation rates than nonporous surfaces.

Published under license by AIP Publishing. <https://doi.org/10.1063/5.0023501>

## I. INTRODUCTION

The current pandemic of Covid-19 has attracted the attention of many researchers to spreading mechanisms of infectious diseases caused by viruses. Airborne microdroplets and aerosols are the primary mode for the spread of many infections including Covid-19, which is caused by the SARS-CoV-2 coronavirus.<sup>1–3</sup> A crucial question is for how long microdroplets can survive when airborne and when deposited on different surfaces subject to varying environmental conditions including the air temperature, relative humidity (RH), and electromagnetic irradiation, such as solar radiation.<sup>4–9</sup> Microdroplets that carry airborne viruses typically have diameters between 1  $\mu\text{m}$  and 100  $\mu\text{m}$ , while deposited droplets may be even larger.

From a physicist's point of view, virus particles (virions) are nanoparticles with a typical linear size from dozens to several hundreds of nanometers (nm). Some viruses have an almost spherical or icosahedron shell (a protein capsid), while others have more complex shapes. Many viruses are also enveloped into a lipid bilayer membrane. The SARS-CoV-2 virion is a sphere with a diameter of about 80 nm surrounded by the lipid envelope (membrane) with structural proteins attached to it. The spike (S) proteins upon the membrane are up to 20 nm long, and scanning electron

microscope (SEM) images of this virus resemble a solar corona, hence the name “coronavirus.” The RNA is contained inside a capsid made of the nucleocapsid (N) protein. The envelope (E) and membrane (M) proteins are attached to the lipid bilayer membrane (Fig. 1).

Viruses do not have their own homeostasis and metabolism; therefore, they are dependent on the environmental conditions. There are numerous indications that viruses get inactivated in dry environments, while they survive in a water environment. Water is required for the self-assembly of virus parts. This is because water facilitates the hydrophobic forces (attracting forces between non-polar molecules and regions of amino acids), which direct the protein folding and the self-assembly of both the protein capsid and the lipid bilayer envelope. While the self-assembly occurs inside an invaded cell, the water environment is still needed to maintain the activity of many viruses providing a more stable thermal environment and hydrophobic interactions.<sup>10</sup> Drying of microdroplets containing virus particles is an effective way of stopping the spread of many viruses leading to protein denaturation and other processes that inactivate the virus.<sup>11–13</sup>

Viruses are also made inactive with heating. Thus, coronaviruses are made inactive at temperatures elevated to 55–60 °C.<sup>5</sup>

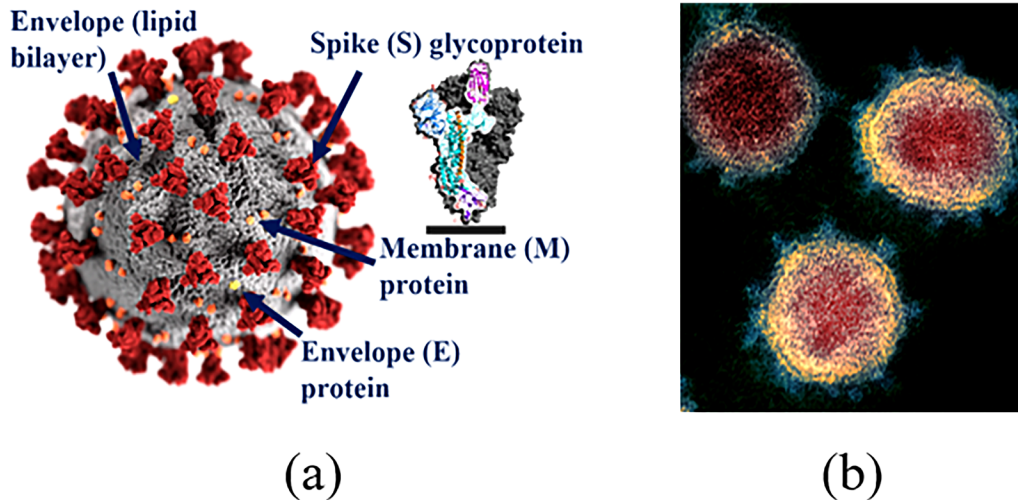


**FIG. 1.** (a) Schematic of the SARS-CoV-2 coronavirus with the spike protein structure shown and (b) electron micrograph of the virus (redrawn from Wikipedia, image credit NIAID-RML).

The underlying mechanism is believed to be the temperature-dependency of the kinetics of inactivation processes. Besides heating, the ultraviolet (UV) radiation at the wavelength of about 253 nm is known to inactivate viruses.<sup>14,15</sup>

Modeling droplet evaporation is a long-standing challenge in physics because the problem is far from being trivial. Several mechanisms can be involved in the evaporation simultaneously, including the heat transfer (an evaporating microdroplet usually cools down), diffusion, molecular kinetics in the boundary layer, and the curvature effect for small droplets.<sup>10,16</sup> It is even more complex when the droplet is a solution of proteins and salts, containing nanoparticles, which is the case for respiratory droplets containing viruses.<sup>12</sup> Moreover, evaporation analysis of such droplets deposited on a rough, micro/nanopatterned, or superhydrophobic surface is an even more challenging task, and it becomes even more complex

when electromagnetic irradiation, such as visible,<sup>17</sup> ultraviolet (UV),<sup>14,15</sup> or infrared (IR) light, is involved.

Antibacterial properties of self-cleaning, superhydrophobic,<sup>18,19</sup> and photocatalytic<sup>20,21</sup> surfaces have been well established. Typically, they rely on reduced adhesion between bacteria proteins and the low energy surface or on certain bio-specific interactions between the proteins embedded into the surfaces and the biological agents. A similar approach can be applied to the design of anti-viral surfaces.<sup>22,23</sup> Another approach that could be explored is the application of water-repellent surfaces that may facilitate drying of droplets, thus decreasing the amount of water needed for virus survival.

In this paper, we will review the approaches to modeling droplet evaporation, and we will develop a new model taking into consideration several effects in combination with potential application to virus-bearing droplets while airborne and while deposited

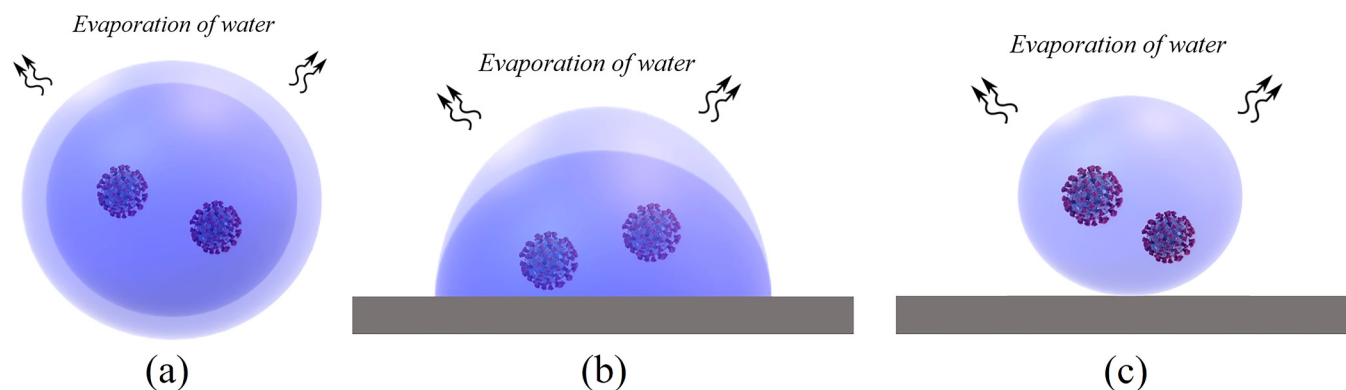


**FIG. 2.** Schematics of evaporation of virus-containing (a) airborne water droplets and droplets on (b) a hydrophilic and (c) a superhydrophobic substrate.

on regular, superhydrophobic, and photocatalytic surfaces (Fig. 2). We will also check the rationality of the model for practical substrates and demonstrate the effect of surface properties (wetting and porosity) on droplet evaporation through experimental observations on novel hydrophobic coatings that were recently developed by our group for potential civil engineering applications.

## II. MODELS OF MICRODROPLET EVAPORATION

In this section, we will discuss various mechanisms of microdroplet evaporation and how environmental factors affect these mechanisms.

### A. Evaporation of airborne water droplets

Evaporation of a liquid involves the change from the liquid phase to the gas phase. At the water–air interface, usually, both evaporation and condensation take place at different rates. Once the air is saturated with water vapor (RH = 100%), evaporation and condensation reach equilibrium. Evaporation prevails over condensation when the surrounding air is unsaturated (RH < 100%).

Evaporation of airborne water droplets has been studied extensively using theoretical, experimental, and numerical models.<sup>24–26</sup> These models are based on several assumptions about the evaporation process, such as the constant temperature assumption, which neglects the temperature distribution within a small droplet. Many models assume that the vapor molecules are removed from the water–gas interface by diffusion. Some models also consider a thin boundary layer referred to as the Knudsen layer with the size on the order of  $1\ \mu\text{m}$  (mean free path of a vapor molecule) at the droplet boundary. For the Knudsen layer model, vapor transport in the layer is governed by Boltzmann's kinetics rather than diffusion.<sup>10</sup> However, the molecular transport from the layer to the ambient is driven by diffusion and by the RH of the ambient. Here, we will develop a simple diffusion-based model without the consideration of the boundary layer.

Let us consider a spherical water microdroplet sprayed in the air. The droplet falling through or floating in the air experiences a drag force that depends on the viscosity of air ( $\eta_a$ ), droplet radius ( $r$ ), and relative velocity of the water droplet with respect to the air ( $v$ ). According to Stokes' law, the drag force can be expressed as  $F_d = 6\pi r\eta v$ . The weight of the water droplet is  $W = \frac{4}{3}\pi(2r)^3\rho_w g$ , where  $\rho_w$  is the density of the water droplet and  $g$  is the gravitational acceleration. Eventually, the drag force on the water droplet equals its weight. Then, the water droplet falls at a constant sedimentation velocity or it flows with the air so that the air velocity relative to the droplet is zero. The relaxation time required to reach the sedimentation velocity for water microdroplets is on the order of a second.<sup>27</sup> The water droplet floating in the unsaturated air undergoes natural evaporation and decreases in size.

Evaporation of a water droplet involves mass transfer from the droplet surface by molecular diffusion. The mass transfer process is coupled with heat transfer. At the initial stage of droplet evaporation, rapid and significant cooling is often observed. At this stage, the heat flux from ambient air is smaller than the required heat for evaporation. Consequently, the droplet temperature is reduced. This initial cooling stage is followed by a longer intermediate evaporation stage when the droplet temperature remains

almost constant. At this stage, the heat flowing from ambient air toward the droplet is equal to the energy required for the evaporation of water. At the final stage of the droplet evaporation, a gradual or abrupt rise in temperature is often observed.<sup>28</sup>

Diffusive mass transport and conduction heat transfer combined with the laws of mass and energy conservation are used to formulate the evaporation model. For the incoming heat flux and the heat loss due to evaporation, the energy balance equation is

$$\rho_w c_w \frac{dT}{dt} = \frac{3k_a}{r^2} (T_a - T) + 3 \frac{\rho_w L_{ev}}{r} \frac{dr}{dt}, \quad (1)$$

where  $T$  is the water droplet temperature,  $T_a$  is the air temperature,  $r$  is the radius of the water droplet,  $c_w = 4.18\ \text{kJ kg}^{-1}\ \text{K}^{-1}$  is the specific heat of water,  $k_a = 0.026\ \text{W m}^{-1}\ \text{K}^{-1}$  is the thermal conductivity of air, and  $L_{ev} = 2.26\ \text{MJ kg}^{-1}$  is the latent heat of evaporation of water.<sup>10</sup> Initially, the temperature of the water droplet can be assumed to be the same as the ambient air temperature. In the initial stage, the droplet radius decreases slowly, and a sharp decrease in temperature is observed.

The mass evaporation rate of the water droplet varies significantly over time. It strongly depends on the saturation vapor pressure and air temperature. It is also proportional to the derivative of the droplet radius. The following mass balance equation presents the mass evaporation rate of a water droplet:

$$\frac{dm}{dt} = -\rho_w \frac{dr}{dt}, \quad (2)$$

$$\frac{dr}{dt} = -\frac{D p_a}{\rho_w r R_a T_a} \ln \frac{p}{p_{sat}}, \quad (3)$$

where  $\frac{dm}{dt}$  is the mass rate of evaporation per unit of droplet's surface,  $D = 3 \times 10^{-5}\ \text{m}^2\ \text{s}^{-1}$  is the diffusion coefficient of air,  $R_a = 286.5\ \text{J kg}^{-1}\ \text{K}^{-1}$  is the universal gas constant of air, and  $p_a = 10^5\ \text{Pa}$  is the ambient air pressure.<sup>10</sup> The rate of droplet evaporation in Eq. (3) does not involve the droplet temperature determined from Eq. (1). This indicates that the diffusion model without the boundary layer involves a significant simplification of the evaporation process.

More accurate models studied in the literature take into consideration the Knudsen layer and, therefore, the effect of droplet's cooling, which may be on the order of 10 K.<sup>10</sup> These models suggested that evaporation is sensitive to both temperature and the RH of ambient air. However, at small and even moderately high levels of RH, microdroplets evaporate within dozens of seconds with the heat flux from the air being the dominant mechanism in every case.

### B. Evaporation of submicrometer-scaled droplets

While most aerosol droplets are larger than  $1\ \mu\text{m}$  in diameter, due to evaporation, the droplet inevitably becomes small. The curvature effect, also known as the Kelvin effect, is significant for submicrometer-scaled droplets.

Evaporating liquid molecules at the surface overcome the bonding and escape from the liquid phase. At a convex curved

surface, the bonding between the neighboring molecules of the dense phase is weaker than that of a flat surface. Consequently, the energy barrier for evaporation decreases. With an increasing curvature of a water droplet, the energy required for the surface water molecules to escape decreases. Consequently, the evaporation rate increases.

For a curved water–air interface, the liquid–vapor equilibrium can be reached at a lower or higher vapor pressure than the saturation vapor pressure. This depends on the sign of the curvature (convex or concave). The sum of the principal radii of curvature referred to as the Kelvin radius,  $1/R_k = 1/r_1 + 1/r_2$ , is realized by the curvature radius. For a spherical droplet, the curvature is always positive (convex interface), and the two principal radii of curvature are equal to each other and to the radius of the droplet; however, for bubbles and concave menisci, the Kelvin curvature may become negative.

The saturation vapor pressure at a convex curved liquid–vapor interface is higher than that of a flat one. To evaluate the partial pressure at the spherical water droplet surface, vapor pressure enhancement due to the droplet curvature needs to be considered. At a certain temperature, the change of the vapor pressure due to the curvature effect is expressed by the Kelvin equation,<sup>29</sup>

$$\ln \frac{P}{P_{sat}} = \frac{2\gamma_{LV}V_m}{rR_aT_a}, \quad (4)$$

where  $\gamma_{LV}$  is the liquid/vapor surface tension and  $V_m$  is the molar volume of the liquid. According to the Kelvin equation, the vapor pressure of the curved surface is inversely proportional to the radius. Smaller droplets evaporate quicker than larger ones due to higher equilibrium vapor pressure. Note that for droplet diameters larger than  $1\ \mu\text{m}$ , the partial pressure of water vapor at the droplet surface is very close to the saturated vapor pressure of the flat surface making the curvature effect negligible. However, the Kelvin effect is significant for submicrometer-sized droplets.<sup>30</sup> At the nanoscale, the Kelvin effect becomes dominant for evaporation or other mass diffusion processes in droplets, water capillary bridges, and menisci.

For a spherical droplet, the equilibrium value of the RH is always greater than 100%, which is the reason why small droplets evaporate even at 100% ambient RH. The rate of evaporation due to the Kelvin mechanism increases proportionally to the difference of the actual curvature of the droplet,  $1/r$ , and the Kelvin curvature,

$$\frac{dm}{dt} \propto \frac{1}{r} + \frac{RT}{2\gamma_{LV}} \ln \frac{p}{p_s}. \quad (5)$$

### C. Role of solutes in water droplet evaporation

While the curvature effect is significant only for submicrometer droplets of pure water, it may become pronounced for much larger droplets, if these contain solutes. Respiratory droplets usually contain proteins and salts occupying a significant fraction of the droplet's volume.

Solute molecules are evenly distributed in a water solution. At the surface, some solute molecules replace some of the water

molecules. Consequently, fewer water molecules are available for evaporation at the water surface. Also, solute molecules are bound with the solvent molecules, which may enhance hydrogen bonding of water molecules. Therefore, the presence of solutes in a water droplet reduces the evaporation rate.

The effect of solutes on droplet evaporation can be interpreted as the diminution of the saturation vapor pressure of the solvent. A solution in which the gas phase has analogous thermodynamic properties of a mixture of ideal gases is called an ideal solution. The diminution of vapor pressure due to the presence of a solute in an ideal solution follows Raoult's law. According to Raoult's law, the vapor pressure of the solution,  $P$ , can be expressed as

$$P = \frac{n_{\text{H}_2\text{O}}}{n_{\text{H}_2\text{O}} + n_s} P_{sat}. \quad (6)$$

Here,  $n_{\text{H}_2\text{O}}$  and  $n_s$  are molar amounts of water and the solute, respectively, and  $P_{sat}$  is the saturation vapor pressure of water. Water solutions follow Raoult's law in the cases of low concentrations of the solute. The reduction of the vapor pressure caused by the dissolved solute shifts the condensation–evaporation dynamic equilibrium at the droplet surface making the saturation vapor pressure smaller than that of a pure water droplet. This also implies that the evaporation rate of the water droplet will decrease with time with decreasing saturation vapor pressure of the solution.

The curvature effect and the solute effect act simultaneously during the evaporation counteracting each other. The Köhler equation<sup>31</sup> describes these two effects in combination correlating the droplet radius to the saturation vapor pressure ratio for a given solute,

$$\frac{P}{P_{sat}} = \frac{n_{\text{H}_2\text{O}}}{n_{\text{H}_2\text{O}} + n_s} \exp\left(\frac{2\gamma_{LV}V_m}{rRT}\right). \quad (7)$$

The effect of the solutes is equivalent to increasing the interfacial curvature radius. For typical values of NaCl and protein concentrations in the respiratory fluids, the equilibrium droplet radius can constitute  $a = 10\ \mu\text{m}$  for RH = 100% and  $a = 1.9\ \mu\text{m}$  for RH = 64%. Smaller droplets would not evaporate. Moreover, for the  $10\ \mu\text{m}$  radius droplet, the time to settle from the 1.5 m height is 8 min, and an inhaled droplet has 81% probability to settle in head airways and only 2% probability to reach the alveolar region of lungs. For the  $1.9\ \mu\text{m}$  droplet, these parameters are 216 min, 57%, and 12%, respectively.<sup>12</sup> Thus, the solute in respiratory microdroplets drastically increases their pathogenic potential.

### D. Surface wetting properties and evaporation of deposited droplets

In this section, the effect of surface properties on naturally evaporating deposited (sessile) droplets will be discussed. Relevant surface properties include the surface roughness, porosity, water absorption capacity, contact angle (CA), and contact angle hysteresis (CAH). Wetting properties characterized by CA and CAH can influence the evaporation process of a sessile droplet significantly.<sup>32</sup> We will now consider naturally evaporating droplets on surfaces of different wettability, such as hydrophilic, hydrophobic, and

superhydrophobic surfaces. The surfaces are assumed nonporous so that the evaporation is the process leading to the disappearance of the sessile water droplets under the isothermal conditions.

The wettability of a solid surface by a liquid is quantified by the contact angle (CA).<sup>33</sup> From Young’s equation, the equilibrium value of the most stable CA,  $\theta$ , is found as

$$\cos \theta = \frac{\gamma_{sv} - \gamma_{sl}}{\gamma_{lv}}, \tag{8}$$

where  $\gamma_{sv}$ ,  $\gamma_{lv}$ , and  $\gamma_{sl}$  are surface tensions (or interfacial free energies) of the solid–vapor, liquid–vapor, and solid–liquid interfaces, respectively.<sup>34</sup> A hydrophilic surface is wetted by water, and a water droplet on it forms a CA  $< 90^\circ$ . For a hydrophobic surface, the liquid–solid contact area is reduced, and wetting is characterized by a CA  $> 90^\circ$ . Surfaces with high CA  $> 150^\circ$  are called superhydrophobic.

Small droplets have a shape of a spherical cap with the diffusion of the vapor in the gas phase dominates over the convection and other heat transfer processes.<sup>35</sup> For a spherical cap shown in Fig. 3(a), the sessile droplet height can be expressed in terms of the contact radius (CR) and the CA,  $\theta$  as follows:

$$h(r, t) = \sqrt{\frac{R^2}{\sin^2 \theta} - r^2} - \frac{r}{\tan \theta}, \text{ where } r \leq R_a. \tag{9}$$

The volume of the evaporating water droplet,  $V(R, t)$ , is given by

$$V(R, t) = \frac{\pi R_a^3}{3} \left( \frac{2 - 3 \cos \theta + \cos^3 \theta}{\sin^3 \theta} \right). \tag{10}$$

Based on the diffusion-controlled mass transfer in the gas phase and considering that the liquid–vapor interface temperature is equal to the ambient temperature, the droplet evaporation rate can be expressed as

$$\begin{aligned} \frac{dV}{dt} &= 2\pi D \Delta P \frac{M}{\rho R T} f(\theta) \left( \frac{3V}{\pi(2 - 3 \cos \theta + \cos^3 \theta)} \right)^{\frac{1}{3}} \\ &\approx 2\pi D \Delta P \frac{M R_a}{\rho R T} \frac{f(\theta)}{\sin \theta}, \end{aligned} \tag{11}$$

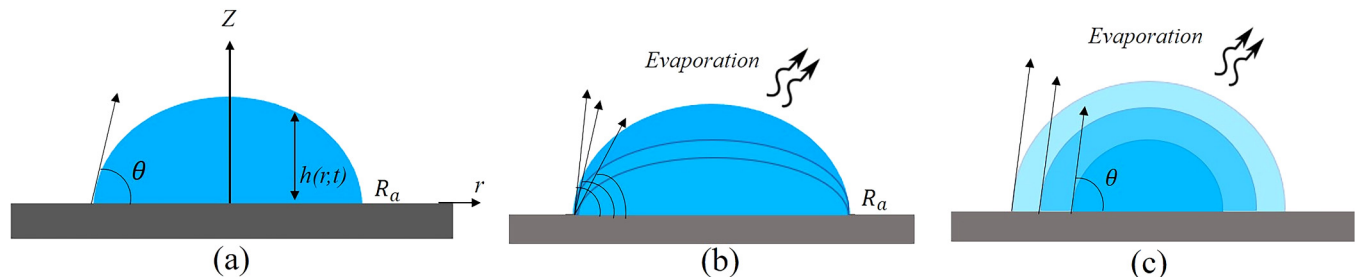


FIG. 3. (a) A sessile droplet on a solid substrate, (b) constant contact radius (CCR) mode, and (c) constant contact angle (CCA) mode of droplet evaporation on a solid substrate.

where  $D$  is the diffusion coefficient of the water vapor molecules in the air,  $\Delta P$  is the difference between the saturation vapor pressure and the ambient vapor pressure,  $M$  is the molar mass of water, and  $f(\theta)$  denotes a geometric factor related to the sessile droplet’s shape. The polynomial representation of  $f(\theta)$  is presented below,<sup>36</sup>

$$\begin{aligned} f(\theta) &= 0.000\,089\,57 + 0.6333\theta + 0.116\theta^2 - 0.088\,78\theta^3 \\ &\quad + 0.010\,33\theta^4 \text{ when } \theta > 10^\circ, \\ f(\theta) &= 0.6366\theta + 0.095\,91\theta^2 - 0.0614\,4\theta^3 \text{ when } \theta < 10^\circ. \end{aligned} \tag{12}$$

The CA and the pinning of the contact line (CL) of the sessile droplet influence the mass transfer and evaporation process. Depending upon the dynamic behavior of the CA and the three-phase contact line (CL), Picknett and Bexon<sup>37</sup> suggested two droplet evaporation modes. The first mode is the constant contact radius (CCR) mode where the CR remains constant and the CA reduces. The second mode is the constant contact angle (CCA) mode when the CA remains constant and the CR decreases with time. Figures 3(b) and 3(c) show the two evaporating modes of a sessile droplet on a solid substrate in ambient air. The transition of these two evaporation modes leads to the change of the sessile droplet’s shape. During the transition, the CL is pinned momentarily and then slips to a new position. Shaikkea *et al.*<sup>38</sup> reported that an intermediate stick-slip mode dominates the final stage of the evaporation of a sessile drop on a solid substrate.

### E. Evaporation of sessile (deposited) droplets on hydrophilic, hydrophobic, and superhydrophobic substrates

The wetting and spreading processes are coupled with the natural evaporation of a sessile droplet on a solid substrate.<sup>39</sup> For complete wetting, the CA is almost  $0^\circ$  and the droplet spreads out completely over the hydrophilic substrate.<sup>40</sup> Lee and co-workers reported that the coupled process of spreading and evaporation of a sessile droplet can be subdivided into two stages for the complete wetting condition.<sup>41</sup> The first stage is short, and the spreading process dominates over negligible evaporation. The volume of the droplet remains approximately constant throughout the first stage. The second stage is comparatively longer, and the CA remains

approximately constant. This stage starts when the spreading process is almost over, and the evaporation process is dominant at this stage.

The evaporation of a sessile droplet on a hydrophilic surface is influenced by the pinning of the three-phase CL in metastable positions due to the chemical and structural heterogeneity of the substrate.<sup>42</sup> The CL pinning is one of the causes of the CA hysteresis (CAH), the difference between the advancing CA and the receding CA. The spreading and evaporation of a sessile droplet undergo four distinct stages.<sup>42</sup> When the droplet is placed on the hydrophilic substrate, the first relatively short stage is characterized by a spreading process.

The evaporation of the sessile droplet can be neglected in this stage. The CA reaches the value of the advancing CA, and the contact radius hits its maximum value. This is followed by the second stage when the CCR mode of sessile droplet evaporation is dominant. The CR remains constant while the CL is pinned, and the CA decreases from the advancing CA to the receding CA value. During the CL pinning, the droplet can have a wide range of CAs maintaining the same CR. In the third stage, the CCA mode of droplet evaporation dominates. The CA remains constant (close to the receding CA) and the CR of the droplet decreases. The fourth and final stage is known as the mixed stage when both the CA and the CR keep decreasing until the droplet disappears. The second and the third stage (CCR and CCA modes of evaporation) last significantly longer than the other two stages constituting 90%–95% of the total drying time. For a hydrophilic substrate, the CCR mode dominates over the CCA.

For a hydrophilic surface ( $CA < 90^\circ$ ), the volume reduction of the sessile droplet in CCR and CCA evaporation modes can be expressed as

$$V(t) = V_0 \left(1 - \frac{t}{t_f}\right)^{\frac{3}{2}}, \quad (13)$$

where  $V_0$  is the initial volume of the sessile droplet and  $t_f$  is the total time of evaporation.

Recent micro/nanotechnological advancements have made it possible to design superhydrophobic surfaces with properties such as water and ice repellence, self-cleaning, and self-healing capacity. Low surface energy coatings combined with micro/nanoroughness are used to synthesize a hydrophobic or a superhydrophobic surface.<sup>43</sup>

Sessile droplets on non-wetting surfaces exhibit different evaporative characteristics compared with those on hydrophilic substrates. One noticeable difference of the droplet evaporation process on a hydrophobic substrate is the negligible duration of the spreading stage than a hydrophilic substrate. The CCA mode of evaporation dominates over the CCR mode due to low CAH and weak CL pinning. CAH is a crucial factor for droplet evaporation, especially on rough surfaces. For the evaporation of sessile droplets on a hydrophilic substrate, the pinning time of the CL takes 75% of the total evaporation time, whereas for hydrophobic substrates, it takes only 40%.<sup>44</sup> For a hydrophilic substrate, the evaporation rate of a sessile drop is linearly proportional to time. However, for hydrophobic substrates, the CCA mode of evaporation dominates, and the evaporation rates are non-linear with respect to time.

Evaporation of a sessile droplet on a superhydrophobic substrate is less well understood. Zhang and co-workers studied the sessile droplet evaporation on a superhydrophobic natural lotus leaf and artificial polymer surfaces.<sup>45</sup> They suggested that the CCR mode of evaporation is dominant on both superhydrophobic surfaces having a hierarchical surface profile. McHale *et al.* studied water droplet evaporation on a superhydrophobic patterned polymer surface. They reported that the water droplet initially evaporated in a pinned CL mode (CCR mode) before the CL recedes in a stepwise fashion.<sup>46</sup> Shin *et al.* reported that a sessile droplet evaporating on a superhydrophobic surface does not have the three distinct modes of evaporation that are common for a hydrophobic surface.<sup>44</sup> Kulinich and Farzaneh studied the effect of CAH on water droplet evaporation from superhydrophobic surfaces.<sup>47</sup> Two types of superhydrophobic surfaces with the same value of CA but significantly different CAH values were used. It was reported that the evaporation of a sessile droplet on superhydrophobic substrates with a low CAH followed the CCA mode. For substrates with a high value of CAH, the CCR mode of droplet evaporation was observed. Droplet evaporation rate was non-linear with time on superhydrophobic surfaces similar to hydrophobic ones.

The unique characteristic of droplet evaporation on a superhydrophobic surface is the absence of CL pinning. A comparatively longer time is required for the evaporation of a sessile droplet on a superhydrophobic surface than on other surface types. The reason behind this is that the water droplet evaporates in the CCR mode maintaining its spherical shape until the final stage of evaporation. This is followed by a reduced evaporation rate when a thin layer is formed before the droplet is completely evaporated. A droplet evaporating on a superhydrophobic surface has a large contact surface area with the air due to the minimum CL pinning. Consequently, it is expected that the evaporation time should be minimum for the superhydrophobic surface, which is opposite to the experimental finding. A likely reason for this is the presence of micro- and nanoscale roughness in a superhydrophobic surface. The surface characteristics and the thin layer formation at the last stage of droplet evaporation become more influential in deciding the duration of the evaporation process.

Porosity, surface patterns, and the wetting state of superhydrophobic surfaces influence the droplet evaporation. The difference between the heterogeneous Cassie–Baxter (trapping of air pockets between the droplet and the surface) and homogeneous Wenzel (complete wetting) states can cause a significant difference in the droplet evaporation process on hydrophilic and hydrophobic surfaces. Superhydrophobic surfaces often have both micro- and nanosized asperities forming the hierarchical roughness.<sup>33</sup> Small sessile water droplets (submicrometer-sized) suspended on a superhydrophobic surface often get deposited between such asperities.

## F. The effect of light radiation

Water is almost transparent for visible light and it does not absorb electromagnetic energy at these frequencies (400 nm–750 nm). The maximum water absorption spectrum is at the wavelength of about  $\lambda = 2.7 \mu\text{m}$ . This infrared (IR) wavelength corresponds to the natural frequency of the O–H bond in the  $\text{H}_2\text{O}$  molecule. However, the solar radiation is extremely weak at this frequency since the majority of the solar light energy is in the visible

light and in the ultraviolet (UV) part of the spectrum. Dombrovsky *et al.*<sup>10</sup> have estimated the average efficiency factor of absorption of solar radiation by microdroplets and found that it is less than 0.05 for droplets of the radius  $R = 50 \mu\text{m}$  or smaller. Therefore, the solar radiation effect on the heating of microdroplets is negligible.

While water is almost transparent, nanoparticles, solutes, and virus particles inside a microdroplet can absorb light radiation and get heated. In this case, the heat exchange of the virus particle with the droplet can become a stabilizing factor, preventing the heating of virions above their inactivation temperature.<sup>14</sup>

As far as the UV part of the spectrum, the wavelength close to  $\lambda = 253 \text{ nm}$  is known to inactivate micro-organisms including viruses because this is a resonance (natural) frequency of nucleic acids. Therefore, solar UV radiation can be used for anti-viral purposes.<sup>14,15,17</sup>

### III. MODELING RESULTS

In this section, we will analyze the evaporation of airborne water droplets and sessile droplets on hydrophilic, hydrophobic, and superhydrophobic surfaces using Eq. (3) for airborne and Eq. (11) for sessile droplets.

The evaporation rates of airborne water droplets with respect to the corresponding droplet radii at a constant temperature ( $20^\circ\text{C}$ ) at different RH levels (RH = 20% and RH = 50%) are presented in Fig. 4(a). The evaporation rate (presented as the rate of the decrease of the radius with time) increases with decreasing droplet radius. At  $20^\circ\text{C}$  and RH = 20%, for an airborne water droplet of an initial radius of  $100 \mu\text{m}$ , the evaporation rate was found to be  $4.7 \times 10^{-4} \text{ m/s}$ , which is consistent with the results found in other studies.<sup>48</sup> A noticeable decrease in the evaporation rate was observed with decreasing RH. The change in the evaporation rate with respect to the droplet radius at a constant RH level (50%) at different temperatures ( $20^\circ\text{C}$  and  $30^\circ\text{C}$ ) is shown in Fig. 4(b). It is found that at the same RH, the evaporation rate is higher at a higher temperature.

The evaporation of a sessile droplet on a surface is a more complicated topic. The evaporation rates of sessile droplets on hydrophilic surfaces as a function of the CA at different RH levels are presented in Fig. 5(a).

The evaporation rate increases with increasing CA. It also increases significantly with decreasing RH. For hydrophilic surfaces, the evaporation characteristics are dominated by the pinning of the three-phase CL. With increasing CA, the contact surface area of air and the droplet increases. Consequently, the evaporation rate also increases. The total evaporation time of sessile droplets on hydrophilic surfaces as a function of CA is presented in Fig. 5(b). For the complete wetting of a hydrophilic substrate ( $CA \approx 0^\circ$ ), the droplet spreads out completely over the surface and forms a liquid film, which takes a significant time to evaporate. However, with increasing initial CA, the total evaporation time decreases due to the increased water-air contact area that intensifies the diffusion process. For hydrophilic surfaces, the CCR mode of sessile droplet evaporation is dominant. In this mode, the contact radius remains constant as the CL is pinned, while the CA decreases from the advancing CA to the receding CA.

The evaporation rates of the sessile droplets on hydrophobic and superhydrophobic surfaces as a function of the initial CA at different RH levels are presented in Fig. 5(c). For hydrophobic surfaces ( $90^\circ < CA < 150^\circ$ ), the evaporation rate increases gradually with the increasing CA. However, for superhydrophobic surfaces ( $CA > 150^\circ$ ), the evaporation rate increases rampantly with the increasing CA. This implies the significant difference between the evaporation processes of a sessile droplet on a hydrophobic and a superhydrophobic surface. For the droplet evaporation on a hydrophobic surface, three modes of evaporation are reported. Among them, the CCA mode is dominant (CA remains constant and the CR decreases). However, for a superhydrophobic surface, the three distinct phases of evaporation do not exist. Stauber and co-workers reported that for strongly superhydrophobic surfaces ( $CA \approx 180^\circ$ ), the CCR and CCA modes are not distinguishable.<sup>49</sup> For a strongly superhydrophobic surface, the CA is the maximum ( $CA \approx 180^\circ$ ), and the contact radius is the minimum ( $R \approx 0$ ). For the evaporation

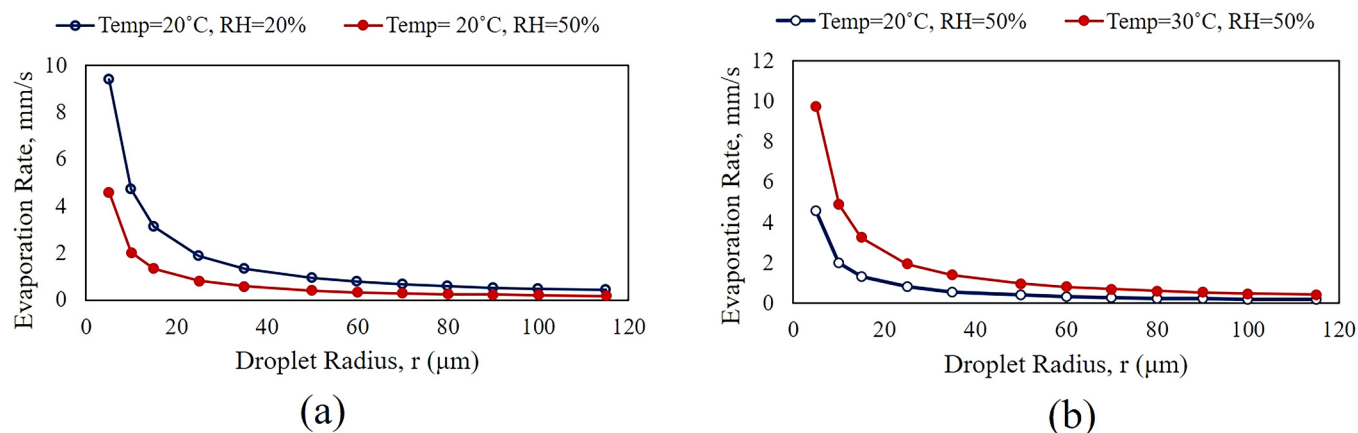
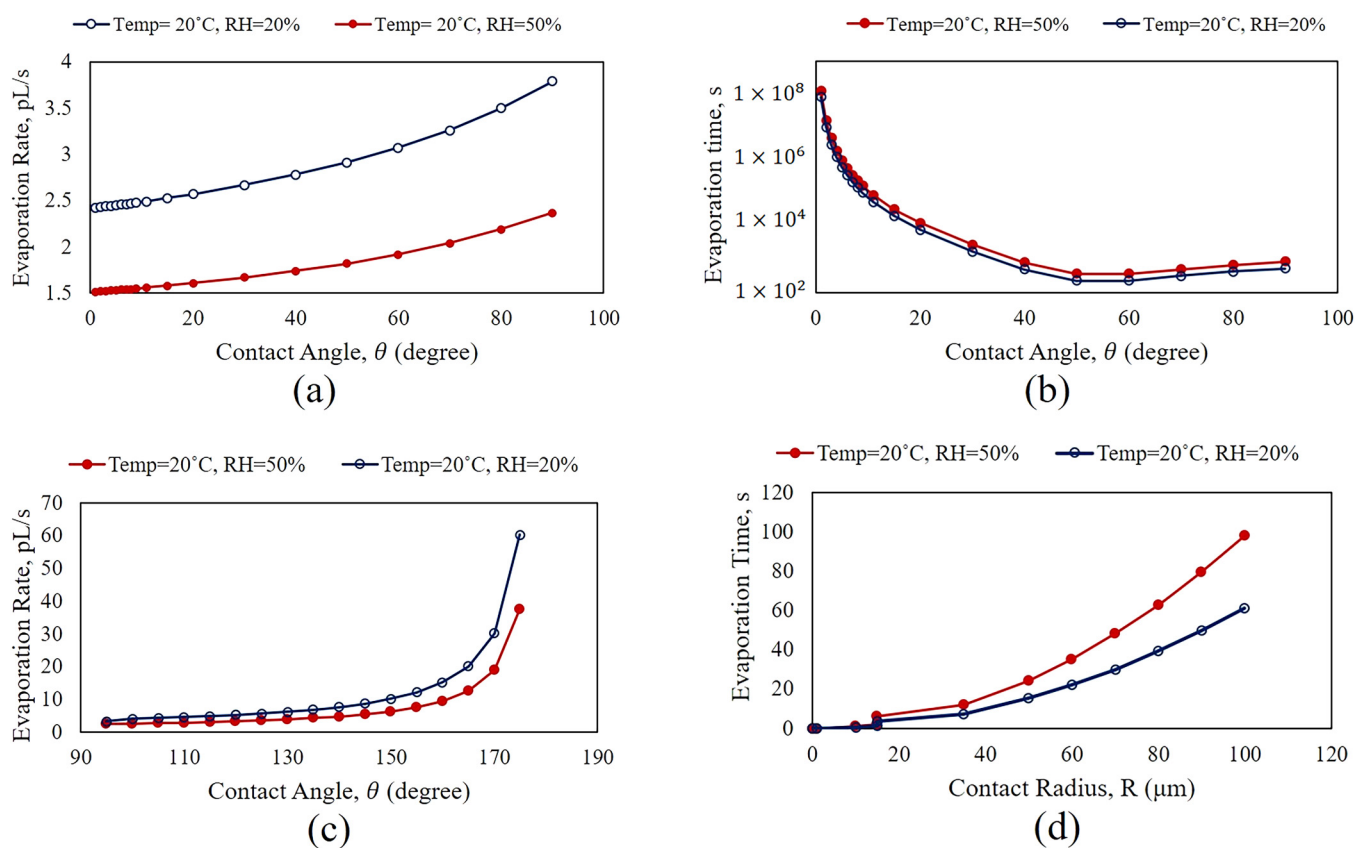


FIG. 4. Evaporation rate vs droplet radius (a) at a constant temperature ( $20^\circ\text{C}$ ) for different RH levels and (b) at a constant RH (50%) at different temperatures.



**FIG. 5.** (a) Evaporation rate and (b) evaporation time vs CA of a sessile droplet ( $R = 10 \mu\text{m}$ ) on a hydrophilic surface, (c) evaporation rate vs CA on hydrophobic and superhydrophobic surfaces at different RH levels at 20 °C, and (d) evaporation time vs radius of sessile droplets on a superhydrophobic surface (CA = 150°) at different RH levels at 20 °C.

of such a sessile droplet in the CCA mode, as the CA remains constant at 180°, the CR is also constant ( $R = 0$ ). Both the CA and the CR remain constant, which makes the two extreme evaporation modes indistinguishable. Also, Fig. 5(c) indicates that the RH level influences the evaporation rate significantly.

The total evaporation time as a function of the CR,  $R$ , of sessile droplets on a superhydrophobic surface (CA = 150°) at different RH levels at 20 °C is presented in Fig. 5(d). The total time for the complete evaporation increases notably with the CR. Also, the evaporation time is higher at a higher RH level at the same temperature.

We studied droplet evaporation using theoretical models. We found that besides RH and air temperature, the evaporation rates depend significantly on the droplet size and surface wetting parameters (for sessile droplets). In Sec. IV, the evaporation of sessile droplets on porous ceramic surfaces will be studied experimentally.

#### IV. EXPERIMENTAL ANALYSIS OF EVAPORATION OF SESSILE DROPLETS

In this section, we will investigate droplet evaporation on photocatalytic and hydrophobic (with a potential to

superhydrophobicity) surfaces. These coatings can be used, for example, as paints on surfaces (such as walls), various public buildings, presumably reducing the rate of virus transmission. Two different types of sessile droplets were considered in the experiments: droplets of de-ionized water and droplets of NaCl–water solution (1.0M concentration). Two different types of surfaces were used: hydrophobic ceramic tile and hydrophobic polypropylene non-woven medical fabrics (fabric of N95 medical mask).

#### A. Superhydrophobic and photocatalytic coatings for concretes and ceramics

Superhydrophobic and photocatalytic coatings for concrete and ceramics are novel technologies for countering the water and ice induced corrosion. Concrete and ceramic are porous and hydrophilic materials with a high water absorption capacity. Incorporating two-layer coatings, superhydrophobic and photocatalytic concrete and ceramic materials can be synthesized. The first layer of the coating is used to chemically bind photocatalytic micro- and nanoparticles (e.g.,  $\text{TiO}_2$ -phosphate) with the substrate to incorporate micro- and nanoroughness. As the second layer, a

low surface energy coating like polymethylhydrogen siloxane (PMHS) or polytetrafluoroethylene (PTFE) is used. With the combination of the micro/nanolevel roughness and a low surface energy coating, the substrate achieves photocatalytic and hydrophobic or superhydrophobic behavior.

## B. Preparation of hydrophobic ceramic tile and polypropylene medical fabric samples

Unglazed clay ceramic tiles (supplied by Blick) were used as the substrate in our experiments. The preparation procedure is discussed in detail in an earlier publication.<sup>43</sup> Two coating layers were applied to flat ceramic tile samples cut to  $50 \times 30 \text{ mm}^2$  size. The first coating layer was a titanium dioxide ( $\text{TiO}_2$ )-phosphate coating. The photocatalytic titanium dioxide-phosphate coated materials are known for their hydrophilicity. When property combined with the strong photocatalytic oxidizing properties of  $\text{TiO}_2$ , the coated ceramic tiles may become self-clean. Hydrophobic modifications were used to transform  $\text{TiO}_2$ -phosphate coated concrete and ceramic tiles to hydrophobic ( $\text{CA} > 90^\circ$ ) and superhydrophobic ( $\text{CA} > 150^\circ$ ) states.

To facilitate the attachment of the  $\text{TiO}_2$  particles to the substrate, phosphoric acid was used as the binder material. A solution of P25 titanium dioxide ( $\text{TiO}_2$ ), phosphoric acid ( $\text{H}_3\text{PO}_4$ ), and water was prepared. The ceramic tiles were dipped into the solution to ensure the application of the first layer of the coating ( $\text{TiO}_2$ -phosphate) evenly on the substrate. After applying the coatings, the tile samples are heat-treated at  $250^\circ\text{C}$  for 1–3 h in a muffle furnace.  $\text{TiO}_2$  particles on the  $\text{TiO}_2$ -phosphate layer produce a micro- and nanoscale hierarchical roughness profile on the tile surface.

A second layer coating of polymethylhydrogen siloxane (PMHS) is applied on the  $\text{TiO}_2$ -phosphate layer to make the ceramic tile samples hydrophobic. The siloxane emulsion is water-based and has several components. For emulsion preparation, a dispersion medium of de-ionized water was used. Polyvinyl alcohol (PVA) was used as a stabilization agent for the emulsion, which

reduces the foam formation. PVA was gradually added to de-ionized water and stirred to prepare the solution. A magnetic stirrer with a hot plate was used to stir the mixture. 25% PMHS and 4.4% surfactant by the weight of the emulsion were used. The concentrations of PMHS and surfactant were maintained precisely. A high-speed mixing at 10 000 rpm was required to stabilize the emulsion. An HSM, model L5M-A from Silverson (a high-speed mixer), was used for this purpose. The emulsion attained hydrophobic properties after almost 24 h of application. After that, it was applied as the second layer of coating for the tile samples.

Five different types of hydrophobic tile samples (R2, R5, R7, R9, and O2) were prepared with different durations of heat treatment, water-acid ratio, and acid/ $\text{TiO}_2$  ratio used in the synthesis. These samples were used for further evaporation of sessile water and NaCl-water solution droplet experiments. Polypropylene non-woven medical fabrics (N95 medical face mask) supplied by Koho Nonwoven Co. were used in the experiments. For preparing the samples, the fabric was cut to  $1 \times 1 \text{ in.}^2$  size. Following the above-mentioned procedures, the two-layer hydrophobic coating was applied to the fabric samples (PP N95).

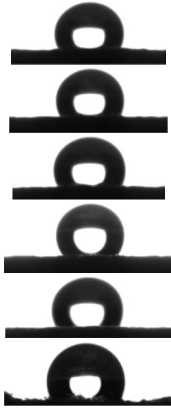
## C. Equipment

The Rame-Hart 250 goniometer was used for measuring the water contact angle (CA). The goniometer has several components: a high-speed camera, light source, micro-syringe, etc. Using the micro-syringe, a sessile water droplet is placed on the sample surface. The camera captures the droplet image, and the “DROPIimage” software of the goniometer analyzes the wetting behavior. The contact angle, droplet radius, deposited volume, etc., can be known from the software.

## D. Experimental procedure

For characterizing the wetting behavior of the samples, CA measurements were done. Using the micro-syringe, three water droplets of the same size ( $4 \mu\text{l}$ ) were placed on each sample at

TABLE I. Contact angle results for different hydrophobic samples.

Sample	Heat treatment duration hour	Water/ $\text{H}_3\text{PO}_4$ ratio	$\text{TiO}_2$ / $\text{H}_3\text{PO}_4$ ratio	Contact angle (deg)	Droplet image
R2	1	20	4	$105 \pm 2$	
R5	1	30	4	$107 \pm 1.5$	
R7	1	30	2	$96 \pm 2$	
R9	3	20	4	$111 \pm 1.5$	
O2	1	23	1	$108 \pm 2$	
PP N95	1	23	1	$108 \pm 2.5$	

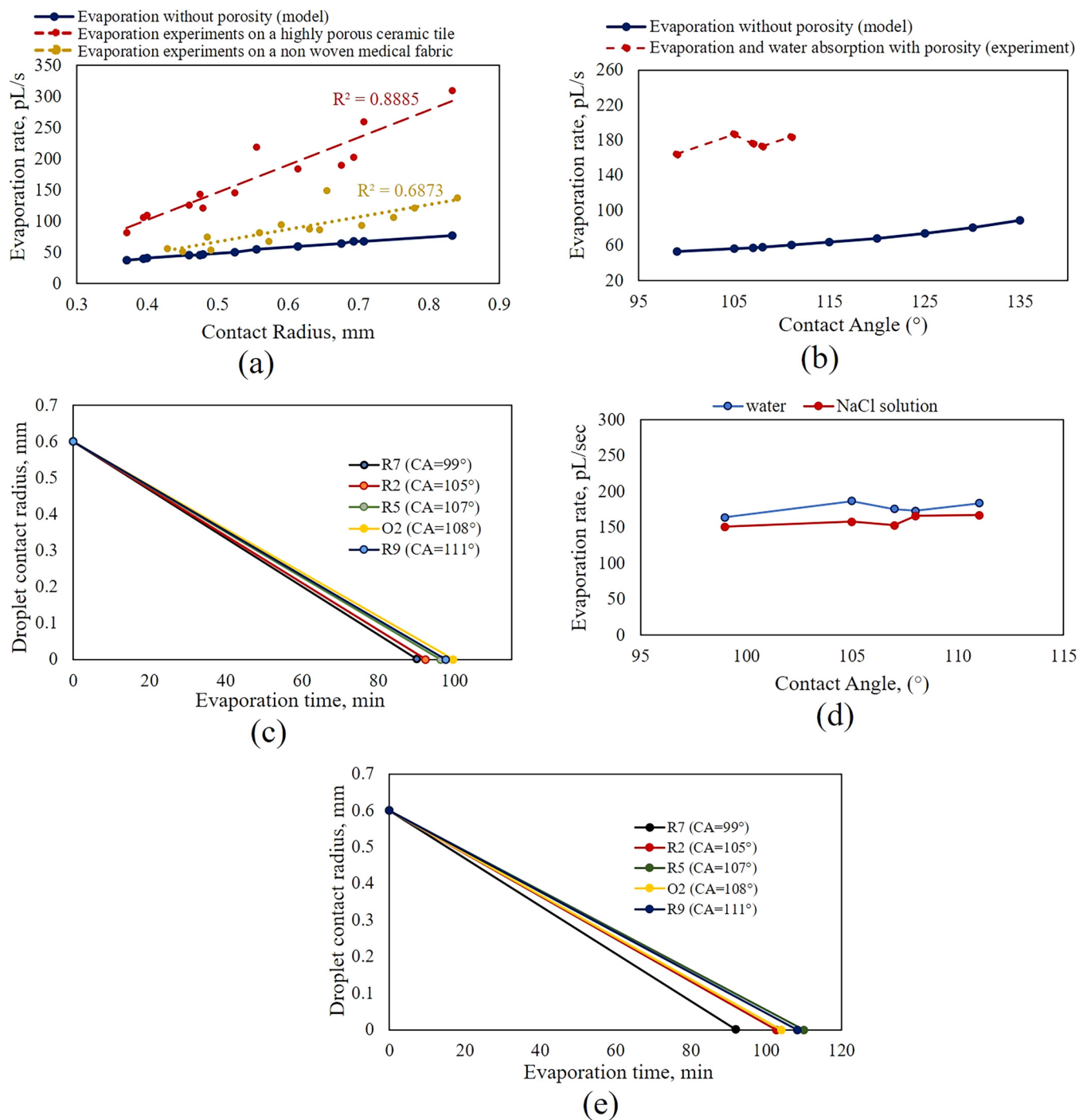


**FIG. 6.** (a) Evaporation rates of sessile water droplets on the O<sub>2</sub> (ceramic tile) and PP N95 (non-woven medical fabric) samples vs the contact radius. The theoretical model is for an ideal nonporous surface (CA = 108°) at 20 °C and 20% RH level, (b) evaporation rate vs CA of water droplets of the same contact radius (CR = 0.60 mm) on tile samples, (c) contact radius vs time required for complete evaporation of water droplets (CR = 0.60 mm) on different ceramic tile samples, (d) evaporation rate vs CA of water droplets and NaCl–water solution droplets (CR = 0.60 mm) on the hydrophobic tile samples, and (e) contact radius vs time required for complete evaporation of the NaCl–water solution droplets (CR = 0.60 mm) on different ceramic tile samples.

different locations. The contact angle values were obtained from the “DROPIimage” software of the goniometer. The average value of the measured contact angles on each sample was considered.

For measuring the evaporation rates of sessile water droplets and NaCl–water solution droplets on the hydrophobic tile samples, droplets of different sizes were placed on different locations of the tile samples. Droplet sizes can be controlled by the micro-syringe. The contact angle, droplet contact radius, and droplet volume were recorded from the “DROPIimage” software of the goniometer. The total evaporation time of different droplets was recorded. Finally, the evaporation rates of sessile droplets on different samples were calculated. In the evaporation experiments, water droplets and NaCl–water solution droplets of contact radius varying from 0.35 mm to 0.85 mm were used.

## V. RESULTS AND DISCUSSIONS

Using the goniometer, the CA on each hydrophobic sample was measured. The CA measurements were performed before the evaporation tests. The CA of different samples ranged between  $96^\circ$  and  $111^\circ$ . Table I summarizes the CA results for different hydrophobic tile samples and the polypropylene medical fabric sample.

The theoretical and the experimental evaporation rates of sessile water droplets on the O2 and PP N95 samples (coated with TiO<sub>2</sub>–phosphate and PMHS hydrophobic layers) are plotted against different CRs in Fig. 6(a). The evaporation rate was estimated as a slope of the volume change with time. From the theoretical model, a linear increment of the evaporation rate is expected with increasing CR (in the range of 0.3 mm–0.9 mm). The evaporation rates from the experimental observations also followed the increasing linear trend with increasing CR. The  $R^2$  values of 0.8885 and 0.6873 indicate that the linear increase of the evaporation rate is a statistically significant approximation for both samples. The experimental evaporation rates on the polypropylene non-woven medical fabric were consistent with the theoretical model. However, the experimental evaporation rates for the highly porous ceramic tiles were observed to be 2.2–4 times greater than the theoretically calculated values for nonporous surfaces.

The water absorption capacity of the highly porous ceramic tile samples is responsible for the deviation between the experimental and theoretical evaporation rates. As far as the imbibition of the porous material, the capillary effects play a significant role only when the external pressure gradient is small enough as compared with capillary forces.<sup>50</sup> The water absorption rate is an important measurement for ceramic tiles. The unglazed ceramic tile samples used in our experiments are highly porous with a high water absorption capacity (more than 6%). During the experiments, two processes (evaporation and water absorption of the tile surface due to porosity) contributed to the disappearance of the droplets. The water absorption capacity of the tile samples also contributed to the reduction of the volume of the sessile droplets. So, less time was required for the disappearance of the droplet due to the additional effect of water absorption of the ceramic tiles. However, in both theoretical modeling and experimental calculation, the effect of porosity, imbibition, or other water absorption processes on the evaporation rate was ignored. Therefore, the experimental evaporation rates of the sessile droplets were higher than the theoretically

predicted values. The size range of the sessile droplets considered in the experiments is also a reason behind the deviation. The theoretical model of evaporation developed here is more effective for small sessile droplets (CR of micrometer range or less). From Fig. 6(a), it is observed that the experimental evaporation rates converge to the theoretical rates with a decreasing CR.

The experimental evaporation rates of the sessile water droplets on different tile samples are plotted against their corresponding CAs in Fig. 6(b). The theoretical model predicts a noticeable increase in the evaporation rates with increasing CA. The range of the CAs of the sample tiles was not wide ( $99^\circ$ – $111^\circ$ ). Yet, the increasing trend of the evaporation rates with increasing CAs was observed from the graph. The evaporation rates on the highly porous tile samples (experimental) were observed to be 2.96–3.15 times greater than the nonporous surfaces (theoretical). The water absorption capacity of the porous ceramic tile samples was the reason behind the higher evaporation rates.

Total time required for the complete evaporation of sessile water droplets on different ceramic tile samples is presented in Fig. 6(c). Water droplets of the same size (CR = 0.60 mm) were placed on different ceramic tile samples to find the evaporation time. For the same CR, the volume of the sessile water droplet increased with increasing CA. The evaporation rate also increased with increasing CA. The graph shows that with increasing CA (in the range of  $99^\circ$ – $111^\circ$ ), the time required for the complete evaporation was also increased.

The experimental evaporation rates of the sessile water droplets and NaCl–water solution (1.0M) droplets on the ceramic tile samples were plotted against the corresponding CAs in Fig. 6(d). In both cases, the evaporation rates increased with increasing CAs. The presence of solutes in a water droplet decreases the evaporation rate. For the same droplet size (CR = 0.60 mm) and the same ceramic tile samples, the evaporation rates of the NaCl–water solution droplets were slightly lower than those of the water droplets.

The time required for the complete evaporation of sessile NaCl–water solution droplets on different ceramic tile samples is presented in Fig. 6(e). NaCl–water solution droplets of the same size (CR = 0.60 mm) were placed on different ceramic tile samples. For the same CR, the volume and the evaporation rate of the droplet increased with increasing CA. From Fig. 6(e), it is seen that with increasing CA (in the range of  $99^\circ$ – $111^\circ$ ), the time required for the complete evaporation of a sessile NaCl–water solution droplet increases.

The experimental study demonstrated that apart from RH and temperature, and droplet size evaporation is greatly influenced by surface properties (wetting and porosity). Surface coatings with desired properties can potentially prevent the spread of viruses by repelling the virus-bearing droplets and inactivating viruses by facilitating microdroplet evaporation.

## VI. CONCLUSIONS

Evaporation of water microdroplets can prevent the spread of viruses because drying causes protein denaturation and other processes that eventually inactivate the virus. We have reviewed modeling approaches for mechanisms of droplet evaporation including diffusion, the Kelvin effect, and the effects of solutes and light radiation for airborne and sessile droplets. Evaporation rates of sessile

droplets on a hydrophobic polypropylene non-woven medical fabric and highly porous ceramic tiles were studied experimentally. Both theoretical modeling and experimental observations demonstrated that temperature, RH, and droplet size affect the evaporation rate. However, besides these factors, surface properties such as wetting and porosity were also significant. The experimental droplet evaporation rates on the hydrophobic polypropylene non-woven medical fabric (coated with TiO<sub>2</sub>-phosphate and PMHS layers) were consistent with the theoretical model. However, the evaporation rates on highly porous samples were 2.2–4 times higher than on nonporous surfaces. Since both porosity and wetting properties affect droplet evaporation, modifications and control of these properties can help inactivate viruses and prevent their spread.

The observed phenomena show the complexity of interactions involved in the evaporation of liquid droplets on surfaces. These interactions involve those inherent to the evaporation itself (heat and mass exchange, diffusion, the dynamic balance of vaporization and condensation) and those typical for the interaction of liquid with rough and porous surfaces (adhesion, pinning, heterogeneous, and homogeneous interfaces). The control of these interactions and surface properties can allow the optimization of droplet evaporation for objectives such as the prevention of spreading of infectious diseases through droplets.

#### ACKNOWLEDGMENTS

This project was supported by the National Science Foundation CBET/Rapid Award No. 2028535.

#### DATA AVAILABILITY

The data that support the findings of this study are available from the corresponding author upon reasonable request.

#### REFERENCES

- <sup>1</sup>L. Bourouiba, *J. Am. Med. Assoc.* **323**(18), 1837–1838 (2020).
- <sup>2</sup>D. Lewis, *Nature* **580**(7802), 175 (2020).
- <sup>3</sup>E. Y. C. Shiu, N. H. L. Leung, and B. J. Cowling, *Curr. Opin. Infect. Dis.* **32**(4), 372–379 (2019).
- <sup>4</sup>N. van Doremalen, D. H. Morris, M. G. Holbrook, A. Gamble, B. N. Williamson, A. Tamin, J. L. Harcourt, N. J. Thornburg, S. I. Gerber, J. O. Lloyd-Smith, E. de Witt, and V. J. Munster, *N. Engl. J. Med.* **382**(16), 1564–1567 (2020).
- <sup>5</sup>J. A. Otter, C. Donskey, S. Yezli, S. Douthwaite, S. D. Goldenberg, and D. J. Weber, *J. Hosp. Infect.* **92**(3), 235–250 (2016).
- <sup>6</sup>F. Girard, M. Antoni, S. Faure, and A. Steinchen, *Colloids Surf. A* **323**(1–3), 36–49 (2008).
- <sup>7</sup>Y. Fukatani, D. Orejon, Y. Kita, Y. Takata, J. Kim, and K. Sefiane, *Phys. Rev. E* **93**(4), 043103 (2016).
- <sup>8</sup>L.-D. Chen, *Int. J. Hyg. Environ. Health* **229**, 113568 (2020).
- <sup>9</sup>S. Chaudhuri, S. Basu, P. Kabi, V. R. Unni, and A. Saha, *Phys. Fluids* **32**(6), 063309 (2020).
- <sup>10</sup>L. Dombrovsky, A. Fedorets, V. Levashov, A. Kryukov, E. Bormashenko, and M. Nosonovsky, *Atmosphere* **11**(9), 965 (2020).
- <sup>11</sup>W. Yang and L. C. Marr, *Appl. Environ. Microbiol.* **78**(19), 6781–6788 (2012).
- <sup>12</sup>L. C. Marr, J. W. Tang, J. van Mellekom, and S. S. Lakdawala, *J. R. Soc. Interface* **16**(150), 20180298 (2019).
- <sup>13</sup>K. Linn and L. C. Marr, *Environ. Sci. Technol.* **54**(2), 1024–1032 (2020).
- <sup>14</sup>C.-C. Tseng and C.-S. Li, *Aerosol Sci. Technol.* **39**(12), 1136–1142 (2005).
- <sup>15</sup>W. A. M. Hijnen, E. F. Beerendonk, and G. J. Medema, *Water Res.* **40**(1), 3–22 (2006).
- <sup>16</sup>R. Bhardway and A. Agrawal, *Phys. Fluids* **32**(6), 061704 (2020).
- <sup>17</sup>C. D. Lytle and J.-L. Sagripanti, *J. Virol.* **79**(22), 14244–14252 (2005).
- <sup>18</sup>X. Zhang, L. Wang, and E. Levänen, *RSC Adv.* **3**(30), 12003–12020 (2013).
- <sup>19</sup>K. Ellinas, D. Kefallinou, K. Stamatakis, E. Gogolides, and A. Tseripi, *ACS Appl. Mater. Interfaces* **9**(45), 39781–39789 (2017).
- <sup>20</sup>J. C. Tiller, C. J. Liao, K. Lewis, and A. M. Klibanov, *Proc. Natl. Acad. Sci. USA* **98**(11), 5981–5985 (2001).
- <sup>21</sup>H. Murata, R. R. Koepsel, K. Matyjaszewski, and A. J. Russell, *Biomaterials* **28**(32), 4870–4879 (2007).
- <sup>22</sup>G. Marinaro, M. Burghammer, L. Costa, T. Dane, F. De Angelis, E. Di Fabrizio, and C. Riekel, *ACS Appl. Mater. Interfaces* **7**(23), 12373–12379 (2015).
- <sup>23</sup>L. Zhang and R. L. Gallo, “Antimicrobial peptides,” *Curr. Biol.* **26**(1), R14–R19 (2016).
- <sup>24</sup>R. Holyst, M. Litniewski, D. Jakubczyk, K. Kolwas, M. Kolwas, K. Kowalski, S. Migacz, S. Palesa, and M. Zientara, *Rep. Prog. Phys.* **76**(3), 034601 (2013).
- <sup>25</sup>V. Y. Levashov, A. P. Kryukov, and I. N. Shishkova, *Int. J. Heat Mass Transfer* **127**, 115–122 (2018).
- <sup>26</sup>O. Carrier, N. Shahidzadeh-Bonn, R. Zargar, M. Aytouna, M. Habibi, J. Eggers, and D. Bonn, *J. Fluid Mech.* **798**, 774–786 (2016).
- <sup>27</sup>H. J. Holterman, *Kinetics and Evaporation of Water Drops in air* (IMAG, Wageningen, 2003), Vol. 2012.
- <sup>28</sup>V. Y. Levashov and A. P. Kryukov, *Colloid J.* **79**(5), 647–653 (2017).
- <sup>29</sup>M. Nosonovsky and P. K. Rohatgi, *Biomimetics in Materials Science: Self-Healing, Self-Lubricating, and Self-Cleaning Materials* (Springer Science & Business Media, 2011), Vol. 152.
- <sup>30</sup>Y. Wang, Y. Yang, Y. Zou, Y. Cao, X. Ren, and Y. Li, *Aerosol Air Quality Res.* **16**(2), 301–313 (2016).
- <sup>31</sup>H. Köhler, *Trans. Faraday Soc.* **32**, 1152–1161 (1936).
- <sup>32</sup>T. A. H. Nguyen, A. V. Nguyen, M. A. Hampton, Z. P. Xu, L. Huang, and V. Rudolph, *Chem. Eng. Sci.* **69**(1), 522–529 (2012).
- <sup>33</sup>M. S. Hasan and M. Nosonovsky, *Phys. Rev. Fluids* **5**(5), 054201 (2020).
- <sup>34</sup>M. S. Hasan and M. Nosonovsky, “Lotus effect and friction: Does nonstickiness mean slippery?,” *Biomimetics* **5**(2), 28 (2020).
- <sup>35</sup>S. Semenov, V. M. Starov, R. G. Rubio, and M. G. Velarde, *Langmuir* **28**(43), 15203–15211 (2012).
- <sup>36</sup>F. Schönfeld, K.-H. Graf, S. Hardt, and H.-J. Butt, *Int. J. Heat Mass Transfer* **51**(13–14), 3696–3699 (2008).
- <sup>37</sup>R. G. Picknett and R. Bexon, *J. Colloid Interface Sci.* **61**(2), 336–350 (1977).
- <sup>38</sup>A. J. D. Shaikha, S. Basu, A. Tyagi, S. Sharma, R. Hans, and L. Bansal, *PLoS One* **12**(9), e0184997 (2017).
- <sup>39</sup>H. Hu and R. G. Larson, *J. Phys. Chem. B* **106**(6), 1334–1344 (2002).
- <sup>40</sup>S. Semenov, A. Trybala, R. G. Rubio, N. Kovalchuk, V. Starov, and M. G. Velarde, *Adv. Colloid Interface Sci.* **206**, 382–398 (2014).
- <sup>41</sup>K. S. Lee, C. Y. Cheah, R. J. Copleston, V. M. Starov, and K. Sefiane, *Colloids Surf. A* **323**(1–3), 63–72 (2008).
- <sup>42</sup>D. Bonn, J. Eggers, J. Indekeu, J. Meunier, and E. Rolley, *Rev. Mod. Phys.* **81**(2), 739 (2009).
- <sup>43</sup>S. Lanka, E. Alexandrova, M. Kozhukhova, M. S. Hasan, M. Nosonovsky, and K. Sobolev, *ASME J. Tribol.* **141**(10), 101301 (2019).
- <sup>44</sup>D. H. Shin, S. H. Lee, J.-Y. Jung, and J. Y. Yoo, *Microelectron. Eng.* **86**(4–6), 1350–1353 (2009).
- <sup>45</sup>X. Zhang, S. Tan, N. Zhao, X. Guo, X. Zhang, Y. Zhang, and J. Xu, *ChemPhysChem* **7**(10), 2067–2070 (2006).
- <sup>46</sup>G. McHale, S. Aqil, N. J. Shirtcliffe, M. I. Newton, and H. Y. Erbil, *Langmuir* **21**(24), 11053–11060 (2005).
- <sup>47</sup>S. A. Kulnich and M. Farzaneh, *Appl. Surf. Sci.* **255**(7), 4056–4060 (2009).
- <sup>48</sup>D. E. Walton, *Drying Technol.* **22**(3), 431–456 (2004).
- <sup>49</sup>J. M. Stauber, S. K. Wilson, B. R. Duffy, and K. Sefiane, *Langmuir* **31**(12), 3653–3660 (2015).
- <sup>50</sup>V. R. Dushin, V. F. Nikitin, N. N. Smirnov, E. I. Skryleva, and V. V. Tyurenkova, *Microgravity Sci. Technol.* **30**, 393–398 (2018).